# On the Suitable choice of Metal for HgTe Nanocrystal-based Photodiode: to Amalgam or not to Amalgam

Rodolphe Alchaar[1], Corentin Dabard[1,2], Dario Mastrippolito[3], Erwan Bossavit[1,4], Tung Huu Dang[1], Mariarosa Cavallo[1], Adrien Khalili[1], Huichen Zhang[1], Lucile Domenach[1], Nicolas Ledos[1], Yoann Prado[1], David Troadec[5], Ji Dai[6], Massimo Tallarida[6], Federico Bisti[3], Fabian Cadiz[7], Gilles Patriarche[8], José Avila[4], Emmanuel Lhuillier[1*], Debora Pierucci[1]

[1] Sorbonne Université, CNRS, Institut des NanoSciences de Paris, INSP, F-75005 Paris, France.
[2] Laboratoire de Physique et d'Etude des Matériaux, ESPCI-Paris, PSL Research University, Sorbonne Université Univ Paris 06, CNRS UMR 8213, 10 rue Vauquelin 75005 Paris, France.
[3] Department of Physical and Chemical Sciences (DSFC), University of L'Aquila, 67100 L'Aquila, Italy
[4] Synchrotron SOLEIL, L'Orme des Merisiers, Départementale 128, 91190 Saint-Aubin, France.
[5] Univ. Lille, CNRS, Centrale Lille, Univ. Polytechnique Hauts-de-France, Junia, UMR 8520 - IEMN, F-59000 Lille, France
[6]CELLS - ALBA Synchrotron Radiation Facility, Carrer de la Llum 2-26, 08290 Cerdanyola del Valles, Barcelona, Spain
[7] Physique de la matière condensée, Ecole Polytechnique, CNRS, Institut polytechnique de Paris, 91128 Palaiseau, France
[8]Centre de Nanosciences et de Nanotechnologies, CNRS, Univ. Paris-Sud, Université Paris-Saclay, 10 Boulevard Thomas Gobert, 91120 Palaiseau, France

**Abstract**: HgTe, thanks to its unique spectral tunability in the infrared is the only material able to cover near, short and mid wave infrared. Current best devices rely on diode electrodes made from transparent conductive oxides and gold, but so far none of these completely fit for purpose. Gold is not compatible with Si foundries and transparent conductive oxides are highly lossy in this spectral range, limiting electrode transparency. Metal based electrodes appear as good alternative candidates but require further investigations. While obvious constraints of work function get raised, chemical stability appears equally important. Here we screen the use of Au, Al, Ag, and Zn as possible metal and reveal that in the case of Ag dramatic transformations of Ag and HgTe are observed. Especially, a cation exchange procedure can occur over a solid-state film without intentional heating of the sample. This process has then been studied combining both structural and electronic probes. This work points out the importance of the careful choice of surrounding electrodes in the case of HgTe since the observed mechanism is likely not limited to Ag. On the other hand, both Au and Al appear stable toward this transformation.

**Keywords**: nanocrystals, HgTe, infrared, photodiode, amalgam.

*To whom correspondence should be sent: el@insp.upmc.fr

## INTRODUCTION

Nanocrystals (NCs), through quantum confinement, offer an exceptional spectral tunability. In the case of HgTe[1], the lack of bulk band gap further expands the electromagnetic range that can span over two orders of magnitude (roughly 1-100 µm) enabling it to cover the whole infrared range. In particular, HgTe is the only material that addresses the 1-5 µm range where many optoelectronic applications occur. This includes telecom applications, active organic sensing (for industrial vision: material sorting, moisture detection…), and passive imaging (mostly defense and astronomy). As basic devices get more mature, the next challenge is now to transfer this technology onto a read-out circuit (ROIC) to design a full imaging setup[2,3]. Some recent high-quality imagers have been proposed, including at wavelengths beyond what can be achieved using PbS NCs[4]. Transfer onto ROIC of NC-based technology raised new questions that have been mostly swept under the rug when designing single pixel in the laboratory. One of them relates to the right choice of metal to design contacts. Gold is commonly used in laboratories but tends to form deep trap states in silicon which makes it banned from silicon foundries. Thus, only post fabrication front end processing of the ROIC with gold is possible. In addition, most vertical geometry devices rely on the use of an electrode that is both transparent and conductive. In the visible range, transparent conductive oxides such as ITO (tin doped indium oxide) or FTO (fluoride doped tin oxide) are intensively used. However, their absorption becomes problematic in the near infrared[5] (**Figure S1**) and prohibitive in the mid-infrared. Certainly, some reports have tried to use either thinner versions of the TCO (transparent conductive oxide)[6,7] but that comes at the price of a higher contact resistance. The replacement of the TCO layer by a metallic grid[7–12] appears as a possible backup strategy to minimize the optical loss and can even possibly generate optical resonances[13].

Usually, the choice of metal for a device is driven by its work function value for a proper ohmic contact design minimizing interface Schottky barriers. In this context, most diodes based on HgTe NCs as active material are currently combining gold as hole extractor and a TCO as electron extractor[14–16]. In consequences, low work function metals are the ones of interest to extract electrons but are also the ones more prompt to oxidation. In the specific context of mercury-based nanocrystals, the high tendency of mercury to form amalgam raised another problem. For example, gold and mercury form well- known alloys in the field of jewelry and dentistry, questioning the current use of gold in HgTe based devices. In this paper, we start by screening the use of different metals (Au, Zn, Al, Ag) as alternatives to TCO electrodes for electron extraction. We observed a dramatic drop in performance in the specific case of Ag whose origins is identified in a coupling between HgTe and Ag layers leading to a long range interdiffusion of the two species. Cation exchange[17] is a well-known process occurring over nanocrystals. Exposure of nanocrystals to cations can lead to an exchange procedure in which the native cations are replaced by those in solution while the anion lattice remains mostly unaffected[18–21]. The procedure was initially developed for a full exchange[22] but rapidly appeared to be more general[23] and has been used to form heterostructures[24,25] or as a strategy to achieve doping[26,27]. The process is nevertheless not limited to nanomaterials and actually has even been used before as a strategy to achieve alloying and doping in bulk II-VI semiconductors. For example, Zn doping can be conducted on HgCdTe[28,29] alloys. However, fairly high temperatures are usually required to obtain such ions interdiffusion in bulk materials. Here, we demonstrate that this phenomenon is particularly effective in the case of Ag bulk metal coupled to HgTe NCs thin film even at room temperature. We give both electronic and microscopic investigations on the process and bring the obtained results in the perspective of a diode design.

## METHODS

**Chemicals**: Mercury chloride ($HgCl_2$, Sigma-Aldrich, 99%), **Mercury compounds are highly toxic. Handle them with special care.** Tellurium powder (Te, Sigma-Aldrich, 99.99%), silver nitrate (Alfa Aesar, 99.9%), $SnO_2$ nanoparticles (15% dispersion in water, Alfa Aesar), trioctylphosphine (TOP, Alfa Aesar, 90%), oleylamine (OLA, Acros, 80-90%), dodecanethiol (DDT, Sigma-Aldrich, 98%), ammonium chloride (Alfa Aesar, 98 %) ethanol absolute (EtOH, VWR), methanol (MeOH, VWR, >98%), isopropanol (IPA, VWR), hexane (VWR, 99%), octane (Carlo erba, 99%), 2-mercaptoethanol (MPOH, Merck, >99%), N,N-dimethylformamide (DMF, VWR), N-methylformamide (NMF, Alfa Aesar, 99%), toluene (VWR, 99.8%). All chemicals are used without further purification except oleylamine that is centrifuged before use.

**1 M TOP:Te precursor**: Tellurium powder (2.54 g) and 20 mL of trioctylphosphine are mixed in a three neck flask. The flask is degassed under sub mbar pressure at room temperature for 5 min and then the temperature is increased to 100 °C. The degassing of the flask is conducted for 20 additional minutes. The atmosphere is switched to nitrogen and the temperature is raised to 275 °C. The solution turns to a clear orange coloration. The heating mantle is removed and the temperature of the flask cools down. Its color changes to yellow. Finally, this solution TOP:Te is used as stock solution and introduced into a glove box for storage.

**HgTe NCs synthesis with band-edge at 6000 $cm^{-1}$**: In a 50 mL three-neck flask, 540 mg of $HgCl_2$ salt and 50 mL of oleylamine are mixed together. The flask is then degassed under reduced pressure at 110 °C. The solution is yellow and clear. Then, 2 mL of TOP:Te (1 M) are extracted from the glove box and are mixed with 8 mL of oleylamine. The atmosphere is replaced by nitrogen and the temperature is set at 57 °C. The pre-heated TOP:Te solution is injected in the three neck flask and the solution turns dark after 1 min. After 3 min, 10 mL of a mixture of 10% DDT in toluene is injected and a water bath is used to prompt the drop of temperature. The content of the flask is split in 4 tubes and MeOH is added. After centrifugation, the pellets are redispersed using 10 mL of toluene in a single centrifuge tube. The solution is precipitated again using absolute EtOH. The formed pellet is redispersed in 8 mL of toluene. At this step, the NCs are centrifuged in fresh toluene to remove the lamellar phase. The solid phase is discarded by centrifugation and the supernatant filtered.

**$Ag_2Te$ NCs synthesis**: In a 50 mL three neck flask, 170 mg of $AgNO_3$ are mixed together with 25 mL of oleylamine and 2.5 mL of oleic acid. The flask is then degassed under vacuum at room temperature for 15 min and then at 70 °C for 10 min. The atmosphere is replaced to nitrogen and 2.5 mL of TOP are added into the solution. Then, the temperature of the flask is raised to 160 °C. After 30 min, the solution becomes orange. At this step, 0.5 mL of TOP:Te (1M) is injected and the reaction is quenched after 10 min with a water bath. The crude solution was stored in a freezer at -20 °C. When needed, 800 µL of the unfrozen crude solution are precipitated with MeOH. After centrifugation the formed pellet is redispersed in a mixture containing 200 µL DDT and 600 µL of chlorobenzene. Then, the NCs are precipitated by addition of methanol. After centrifugation the pellet is dispersed using 800 µL of chlorobenzene. Again, the NCs are precipitated by addition of MeOH and centrifugation. The pellet is this time dispersed in 1.6 mL of a (9:1 volume ratio) mixture of hexane:octane.

**HgTe ink preparation:** $HgCl_2$ (30 mg) is dissolved in a solution of 18 mL of DMF and 2 mL of mercaptoethanol. At each step, the solution is stirred with a vortex and an ultrasonic bath. HgTe nanocrystal solution (900 µL) is mixed with 0.6 mL of the exchange solution and 0.4 mL of DMF. Finally, toluene is added up to reach a global volume of 4 mL and the solution is centrifugated for 2

min at 6000 rpm to precipitate the nanoparticles. The supernatant is discarded, and the formed pellet is dried using nitrogen flux and then redispersed in 200 µL of DMF to target a thickness of about 200 nm. The obtained solution is called ink.

**$SnO_2$:** For lightly doped $SnO_2$, we dilute 200 µL of $SnO_2$ commercial solution with 1 mL of 24 mM $NH_4Cl$ solution in deionized water. For heavily doped $SnO_2$ we dilute 200 µL of commercial solution with 1 mL of 48 mM $NH_4Cl$ solution in water.

**FTO etching:** The FTO-coated (80 nm) glass substrate is cleaned by sonication in acetone then rinsed with isopropanol and dried with an $N_2$ gun. A final cleaning is made using an $O_2$ plasma. An adhesion promoter (TI-Prime) is spin-coated onto the substrate and baked at 120°C for 2 min. AZ5214E is spin-coated and baked at 110°C for 90 s. A standard photolithography process is performed using mask aligner for exposing the substrate to UV light for 20 s through a lithography mask. Photoresist is developed using AZ 726 developer for 30 s and immediately rinsed with deionized water. The FTO is then etched using reactive ion etching (RIE) for 5 min. After etching, the resist is lift-off by dipping the substrate into acetone for a few minutes before finally rinsing with isopropanol and drying with $N_2$.

**Bottom metal electrodes:** The glass substrate is cleaned by sonication in acetone then rinsed with isopropanol and dried with an $N_2$ gun. A final cleaning is made using an $O_2$ plasma. TI-Prime is spin-coated onto the substrate and baked at 120°C for 2 min. AZ51214E is spin-coated and baked at 110°C for 90 s. The substrate is exposed to UV light for 1.5 s through a quartz mask. An inversion baking step for the photoresist is performed at 125°C for 2 min. The substrate is exposed a second time to UV light for 40 s without a mask. The photoresist is developed using AZ726 for 30 s and rinsed with deionized water. For metal electrodes, a 10 nm Ti adhesion layer is evaporated on the substrates, followed by the deposition of an 80 nm layer electrode by thermal evaporation for Au, Ag and Al, and sputtering for Zn. After metal deposition, the resist is lifted-off by dipping the substrate into acetone for a few minutes in order to reveal the metal grating pattern, before finally rinsing with isopropanol and drying with $N_2$.

**Diode with FTO or metal/$SnO_2$/HgTe/$Ag_2Te$/Au stack:** The patterned substrate is sequentially cleaned in acetone and isopropanol. The lightly doped $SnO_2$ solution is deposited onto the substrate, followed by the heavily doped $SnO_2$ solution via spin coating at 4000 rpm for 30 s. The film is annealed on a hot plate at 70°C for 1 h. The HgTe nanocrystals ink is deposited onto the $SnO_2$ film via spin coating at 700 rpm for 120 s followed by a drying step at 2000 rpm for 60 s to target a thickness around 200 nm. The HgTe film is dried under vacuum for at least 2 hours. On top of the HgTe ink film, an $Ag_2Te$ nanocrystals layer is spin-coated at 1500 rpm for 30 s followed by a treatment of $HgCl_2$ (10 mM in methanol) which was dropped onto the film and spin-dried after 15 s. The film is then rinsed with isopropanol. The $Ag_2Te$ spin-coating and treatment steps are repeated one more time. Then, an ethanedithiol (EDT) ligand-exchange is performed by dipping the film in a solution of 1% EDT in acetonitrile for 30 s before being rinsed with pure acetonitrile. Finally, an 80 nm Au top electrode is deposited using thermal evaporation.

**Diode characterization:** Photodiodes were characterized at room temperature. The samples were connected to a Keithley 2634B source-meter that applies bias and measures the current. The measurements were carried out at dark conditions and under illumination. For measurements under illumination, we used a 1.55 µm laser diode (Thorlabs TCLDM9). Neutral density filters (NUK01) were used to reduce the incident laser power and perform measurements at a different laser power.

**Raman spectroscopy:** Raman measurements were conducted at room temperature using a Horiba JobinYvon LabRAM HR confocal Raman microscope with a 100× objective and a 633 nm laser excitation. Spectra were recorded between 80 and 400 $cm^{-1}$ with 1800 lines/mm grating resulting in a resolution of 1 $cm^{-1}$. Spectrometer calibration was set using the 520.5 $cm^{-1}$ band of a Si crystal. The effective laser power at the exit of the objective was about 0.5 mW.

**Focus ion beam slicing**: TEM preparations were performed on Zeiss Crossbeam 550 with Gallium ion source. A protect layer of platinum (35x3 $\mu m^2$) is deposited at 3 nA above the region of interest before etching a surface of 40x12 $\mu m^2$ at each side of the platinum overlayer at 30 nA to a depth of 10µm. A lamella is partially dissociated from the sample at 7nA, only a small bridge remains on one side of the lamella. This lamella is transferred from the sample to the TEM grid with Kleindiek micromanipulator. 1x1 $\mu m^2$ platinum is deposited at 50 pA between the lamella and the tip of micromanipulator. Then the bridge is etched and the lamella transferred to a M- shape cupper grid and fixed by two 300 pA platinum depositions (4x3 $\mu m^2$) on the bottom corners. Thinning of the lamella thickness is composed of three steps with decreasing intensity (700, 100 and 50 pA). The last step consists in limiting the amorphization on each side of the lamella by a low voltage etching (1 kV – 50 pA).

**TEM EDX:** A drop of diluted NCs solution was drop-cast onto a copper grid covered with an amorphous carbon film. The grid was degassed overnight under secondary vacuum. Imaging was conducted using a JEOL 2010 transmission electron microscope operated at 200 kV. Complementarily, TEM/STEM observations were made on a Titan Themis 200 microscope (FEI/Thermo Fischer Scientific) equipped with a geometric aberration corrector on the probe. The microscope was also equipped with the "Super-X" systems for EDX analysis with a detection angle of 0.9 steradians. The observations were made at 200 kV with a probe current of about 50 pA and a half-angle of convergence of 17 mrad. High-angle annular dark-field scanning transmission electron microscopy (HAADF-STEM) images were acquired with a camera length of 110 mm (inner/outer collection angles were respectively 69 and 200 mrad).

**X-ray diffraction (XRD)** signals of thin films of nanoparticles drop-cast on a silicon substrate are recorded on a Phillips X'Pert diffractometer with a Cu-K$\alpha$ radiation. Measurements are performed at a working condition of 40 kV in voltage and 40 mA in current.

**X-ray photoemission spectroscopy**: XPS measurements were performed at LOREA beamline (ALBA Synchrotron facility -Spain). The photon source was APPLE II helical undulator set to deliver linear polarized light. The photon energy was selected using a high-resolution varied-line spacing grating monochromator, with a resolving power $E/\Delta E > 10^4$ in the whole photon range. The end station is equipped with an MBS A-1 hemispherical electron analyzer. All measurements were conducted at room temperature using constant pass energy (PE= 50 eV) within the detector with a photon spot size of about 20 x 20 $\mu m^2$. The acquired data were processed using Wavemetrics Igor Pro: a Shirley/linear background was subtracted and Voigt curves (*i.e.* the convolution of a Gaussian by a Lorentzian) were used for the fitting. The zero binding energy (BE) (*i.e.* the Fermi level) was taken at the leading edge of a clean Ag film.

## RESULTS AND DISCUSSION

To show the generality of the problem we aim to discuss, we start with the diode stack which is currently the most used for HgTe NCs based device, the latter being able to cover both short[14–16,30] and mid wave infrared detection[31] but also being used for electroluminescence[7]. It consists of the combination of HgTe NCs with $Ag_2Te$ NCs, the latter being afterwards cation exchanged to form an

Ag doped HgTe layer. Regarding the electrodes, gold is used as hole extractor due to its high work function. On the electron side, an electron extraction layer can be added depending on the targeted spectral range and is generally coupled to a TCO layer, as schematized in **Figure 1**a. Here, we compare the effect of a continuous layer of FTO with a metallic grid made of Au, Ag, Al or Zn: a series of metals that can easily be evaporated and found in most laboratory setups. Platinum has been excluded since unsuitable for electron extraction because of its high work function. In addition, its high cost prohibits a cost-effective device development.

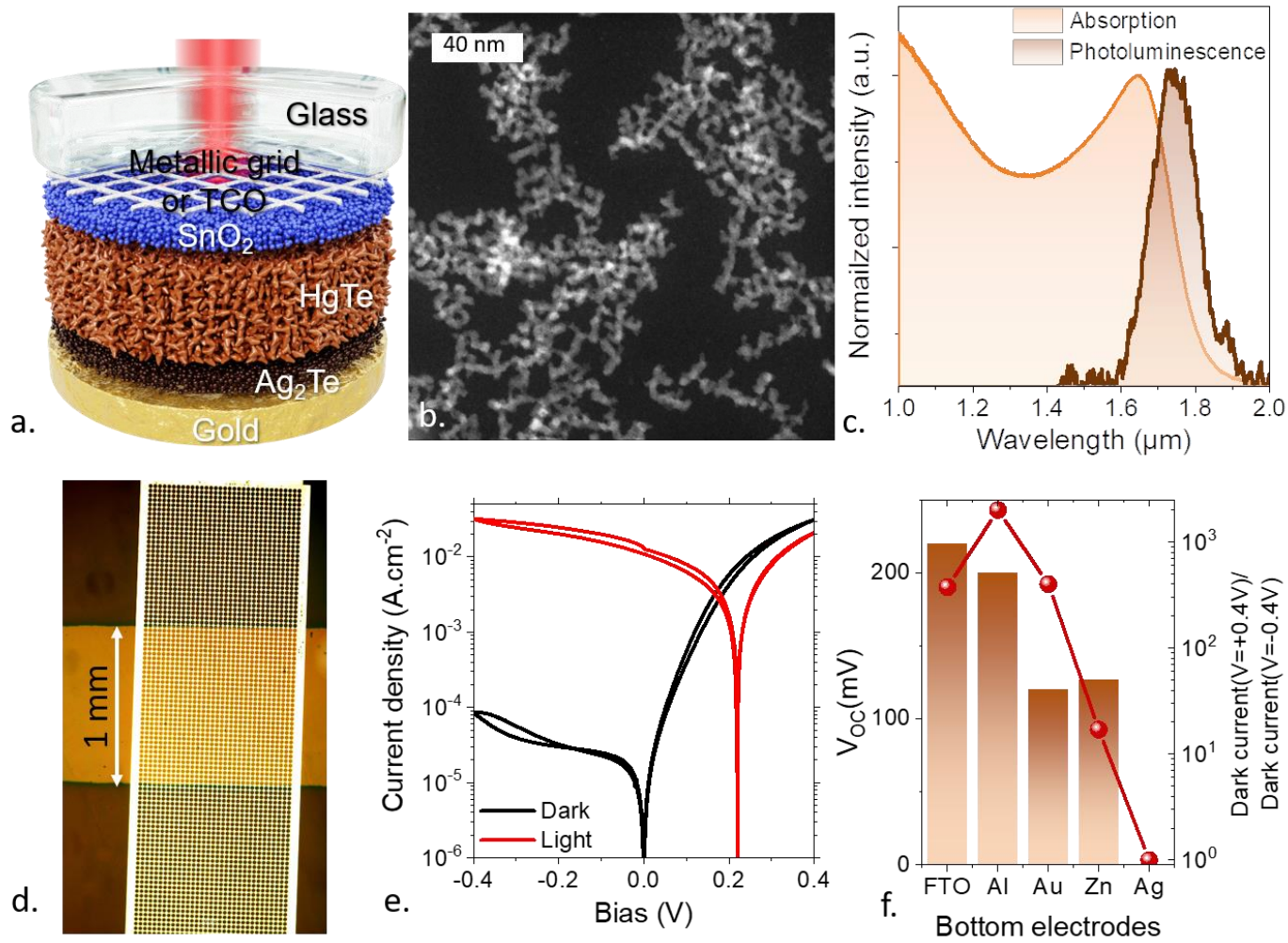


***Figure 1:*** *Schematic of an infrared photodiode in which the bottom electrode can be either a transparent conductive oxide or a metallic grid. b. TEM image of HgTe NCs. c. Absorption and photoluminescence spectra of SWIR HgTe NCs. d. Optical microscope image of the diode through its bottom metallic grid electrode. e. IV curves in the dark and under illumination (λ=1.55 µm – Power=4 mW) by a laser diode in the case where the bottom electrode is made of FTO, also see Figure S2 for the IV curves with metallic grids. f. Open circuit voltage and current asymmetry (ratio of current in the dark under +0.4V and -0.4 V) for various bottom electrodes.*

The active layer is here made of HgTe NCs prepared using Keuleyan's procedure[32]. The size of the particle, around 8 nm according to scanning transmission electron microscopy (STEM, see **Figure 1**b), is chosen to generate a band edge around 1.7 µm (absorption maximum) by the end of the synthesis, see **Figure 1**c. After ligand exchange, conducted to increase the thin film mobility, the cut-off wavelength will be brought at 2 µm, which is relevant to design a sensor with expanded spectral range compared to conventional InGaAs sensor. To ensure that the metal used as bottom electrode is partly transparent, we used a grid with an overall transmission of 85 %. Here the pattern of this grid is large (period 13.5 µm), to avoid any optical resonance effect which is out of the scope of this study. For short wave infrared materials, at room temperature, the IV curve associated with

the device presents a strongly rectifying behavior (>$10^3$ in current asymmetry), see **Figure 1**e for the case of a FTO electrode and Figure S1 for all the metallic grids. Under illumination, the minimum of conductance is clearly shifted and the measured open circuit voltage ($V_{OC}$) reaches 220 mV (≈1/3 of the band gap) under 4 mW of optical power. When using Au, Al and Zn metals, the rectifying behavior is maintained for all of them. In the case of Au, the voltage reduction (of 120 mV, **Figure 1f and S2**), can be explained by the reduced asymmetry of the diode stack (Au being used on both sides) that disfavors the formation of a built-in electric field. With Al most of the performance that was obtained with FTO is maintained, see **Figure 1**e, with a similar open circuit voltage and even improved current asymmetry. This is somehow a bit unexpected due to the high tendency of Al to form alumina, which may have reduced the overall current magnitude. So far, this makes Al the best alternative metal to TCO. However, from experience, oxidation of Al is generally observed when trying to use aluminum to generate plasmonic grating, since optically speaking Al tends to behave more like alumina. In the case of Zn (Figure S1d), we observe an overall drop in the sample conductance and a reduction by half of the open circuit voltage. Zn is also prompt to form oxide but ZnO is also often used as an electron transport layer in NCs based devices, making its formation even possibly beneficial. However, compared to $SnO_2$, ZnO presents a lower electron affinity making it less compatible with the relatively deep band of HgTe[16]. More surprising is the case of Ag for which the IV curve turns completely linear and the open circuit voltage is entirely lost, see **Figure 1**f and S1c. This result is at first glance quite surprising since Ag, Al and Zn present very close work functions (4.2eV ±0.1 eV), thus the observed effect cannot be attributed to any Schottky contact formation.

From the macroscopic point of view, we observe that silver contacts on the diode tend to present darker edges, suggesting a possible chemical transformation of the material. To investigate this effect, we deposited films of the different metal on a Si wafer and on HgTe NC film coated Si wafers, see **Figure 2**a. On the Si wafers, Au presents a standard gold aspect, while the three others show a grey colored reflective aspect. The overall appearance is mostly maintained for Au, Al and Zn once coated on HgTe NCs film, however we indeed observe a change for Ag which switches from a neat grey to a darker shade. We then focus only on Au (because of its actual stability as later shown) and Ag. Raman spectroscopy (**Figure 2**b) brings first evidence of the chemical change occurring in this system. The film of HgTe coated with Au displays the expected vibrational features for HgTe at 92, 123 and 140 $cm^{-1}$ attributed to the LA, TO and LO phonons respectively. A weaker 2LO phonon mode also appears at around 270 $cm^{-1}$ [33]. None of these modes are observed in the film with Ag coating suggesting a strong chemical reorganization of the sample.

X-ray diffraction gives a first clarification of the actual transformation. HgTe NCs are initially grown in a zinc blende phase that exhibits three main diffraction peaks, see **Figure 2**c, corresponding to the (111), (220) and (311) planes. Once coated with an Au layer, the diffractogram appears as the sum of Au and HgTe diffractograms, see the middle part of **Figure 2**c. Bulk metal Au and Ag have close diffraction patterns, showing mostly the same (111) and (220) of the faced center cubic crystal phase, which are shifted with respect to their different lattice parameter. However, the X-ray diffractogram obtained from Ag coated HgTe NCs film is far more complex than the sum of the two phases as observed for gold. Though the presence of a peak at 2θ=23° may have suggested the presence of HgTe, the complete lack of feature at 2θ=46°, corresponding to the expected direction for the (311) peak, first brings evidence that HgTe is no longer present in the system. Analysis of diffractogram is given in **Figure S3** and brings evidence of three phases: metallic Ag (peak at 38°), $Ag_2Te$ (feature at 23°) and Ag/Hg amalgam phase with high Hg content[34] (peak at 31°). In other words, in absence of elevated temperatures (beyond the thermal evaporation), HgTe in contact with

Ag is transformed to $Ag_2Te$ while the metal forms an amalgam with a stoichiometry that depends on the relative amount of the two of them.

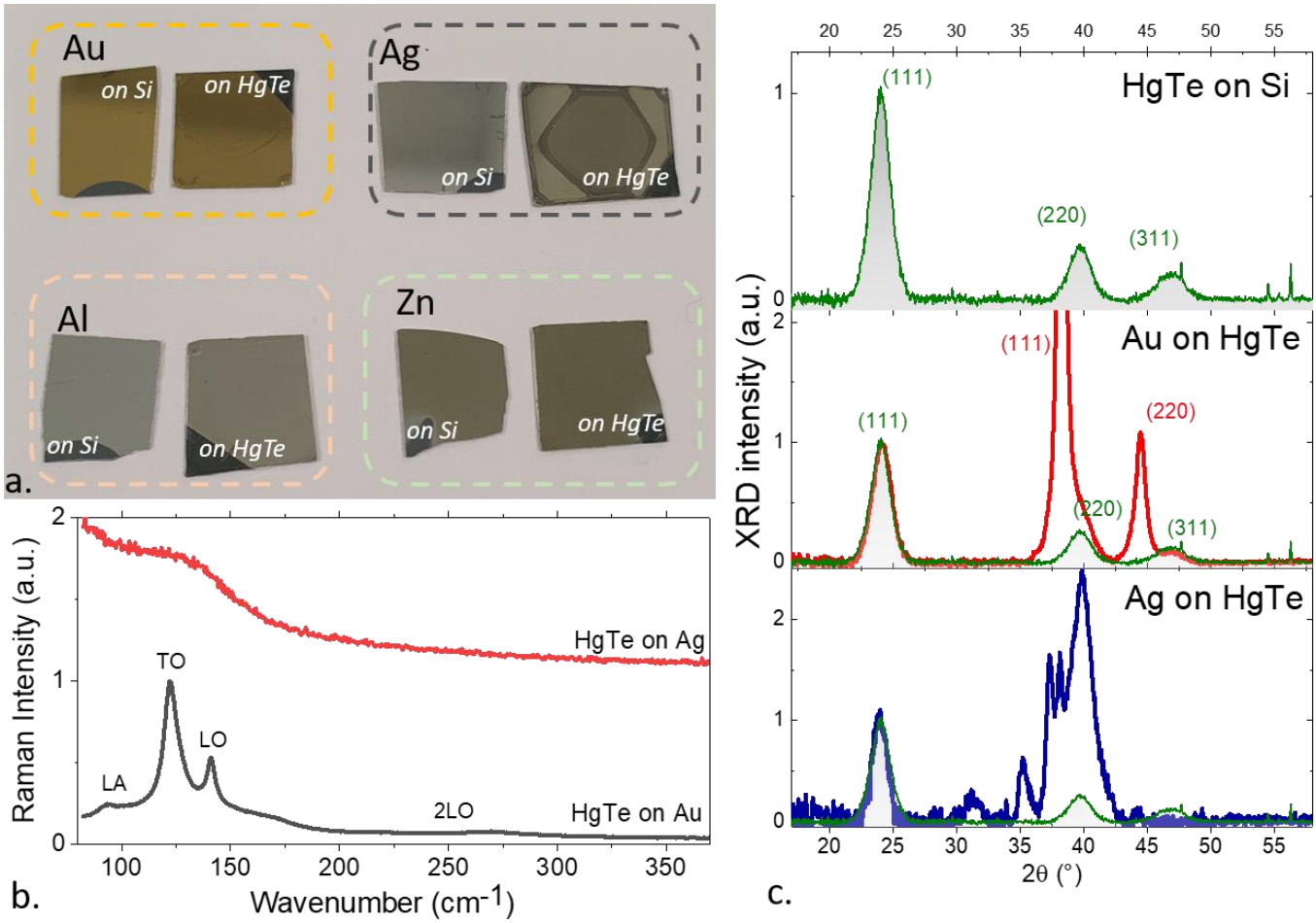


***Figure 2 :*** *a. Image of different metallic films deposited on Si wafers and on a HgTe NC film (200 nm) coated on the Si wafers. Ag film on HgTe presents an obvious change of color compared to metallic Ag. b. Raman spectra for HgTe NC film deposited on Au and Ag. c. X-ray diffraction patterns for HgTe/Si (top graph), HgTe/Au (middle graph) and HgTe/Ag (bottom graph). Also see Figure S2 for analysis of the HgTe/Ag diffractogram. In the middle and bottom parts, the diffractogram of pristine HgTe (green line) has been added as guideline.*

Though the use of Ag nanoparticles is an established method to capture solvated $Hg^{2+}$ ions[18–20], the observed transformation is somehow unexpected at such low temperatures and while the two materials cannot interpenetrate each other. We thus further investigated how the electronic properties of the system get affected using X-ray photoemission spectroscopy (**Figure S4-S6**). According to the photon energy range used (between 400-600 eV), this surface sensitive technique probes less than 1 nm below the surface. Since Raman spectroscopy and X-ray diffraction have established the stability of HgTe coupled to Au, we later used this system as reference. In **Figure 3**a, the photoemission spectra in the lower binding energy range (i.e., close to the valence band maximum) is shown. In the case of HgTe on Au, two main features are present, the Hg 5d core level whose binding energy is around 8.2 eV and the valence band close to the Fermi level. For HgTe on silver, the Hg 5d core level is almost completely suppressed, suggesting that Hg moves away from the surface. However, the film of HgTe on silver now presents a feature that comes from Ag (i.e., signature of Ag 4d states[35,36] in the valence band, similar to the Ag 4d signal observed in silver chalcogenides[37] or to the feature observed from Ag on Si and Ag on HgTe) with a binding energy at

around 6 eV, see **Figure 3**a. Since the Ag is supposed to be located 200 nm underneath the HgTe surface, it can only be detected by photoemission if it has reached the top surface through intermixing with the HgTe NCs.

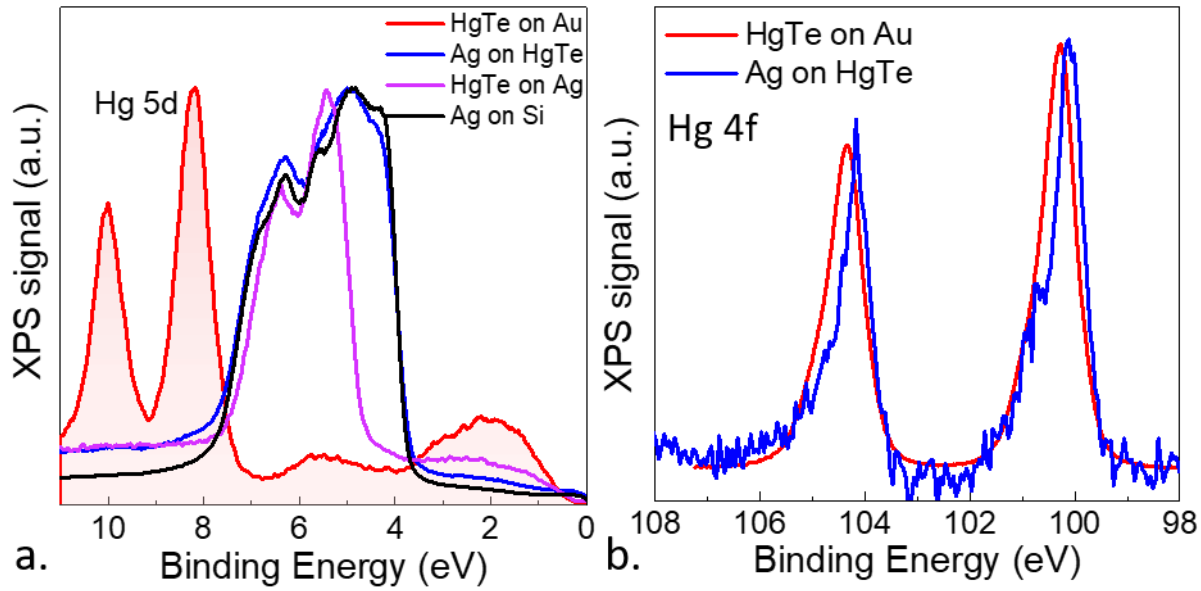


***Figure 3*** *a. Low energy photoemissions spectra for HgTe on gold (used as reference), Ag on HgTe, HgTe on Ag and Ag on Si (hv = 600 eV). b. Hg 4f core levels for HgTe on Au and Ag on HgTe (hv = 473 eV). Deconvolution of the spectra are given in figure S3 to S4.*

This intermixing behavior is furthermore supported by the fact that we were able to detect the Hg 4f core level (higher cross section than the Hg 5d) even when 80 nm of Ag was deposited on top of the HgTe NCs (see **Figure 3**b). The spectrum of the Hg 4f states broadens, compared to the spectrum collected on Au, and in particular displays a new feature at lower binding energy. Proper deconvolution of the spectrum (Figure S3) shows a contribution that can be attributed to $Hg^0$ (possibly under an amalgam form as suggested by XRD). Symmetrically, see Figure S7, the Ag 3d states also displays a new contribution that we attribute to the formation of $Ag_2Te$ bonds. Other metals (Au, Al, and Zn) do not show evidence of formation of metal chalcogenides. Likely in the case of Zn and Al, the oxide may behave as protective layer, see Figure S8-S10. However, the choice of ligand capping the HgTe (thiol, acid amine) does not seem to impact the amalgam formation since the latter is observed in all cases, see figure S11-12.

To spatially quantize this transformation, we have then used energy dispersive X-ray spectroscopy (EDX) conducted on a slab of film sliced by focus ion beam. In the case of Au film on HgTe, see Figure S13, EDX confirms the initial targeted stacking with an Au layer deposited on the top of HgTe NC film layer. Each interface is sharp and there is no evidence for species interdiffusion. As it can be anticipated from previous experiments, the case of Ag on HgTe is quite different, see **Figure 4**. The structure consists of 200 nm coating of HgTe NC film on which we evaporate 80 nm of Ag. STEM image already shows the presence of intriguing inhomogeneous bubbles (see mark 2 in Figure 4). The Ag that is initially located on top of the HgTe film diffuses over the whole volume of HgTe (i.e., over 200 nm). EDX reveals a 2:1 Ag:Te stoichiometry (see mark 1 in **Figure 4**), consistent with formation of an $Ag_2Te$ phase, confirming what was suggested by X-ray diffraction. Within the experimental resolution, the layer is free of Hg. The “bubbles” (see mark 2 in **Figure 4**) appear to be made of an Ag/Hg amalgam with possibly some sulfide content (likely under thiol form).

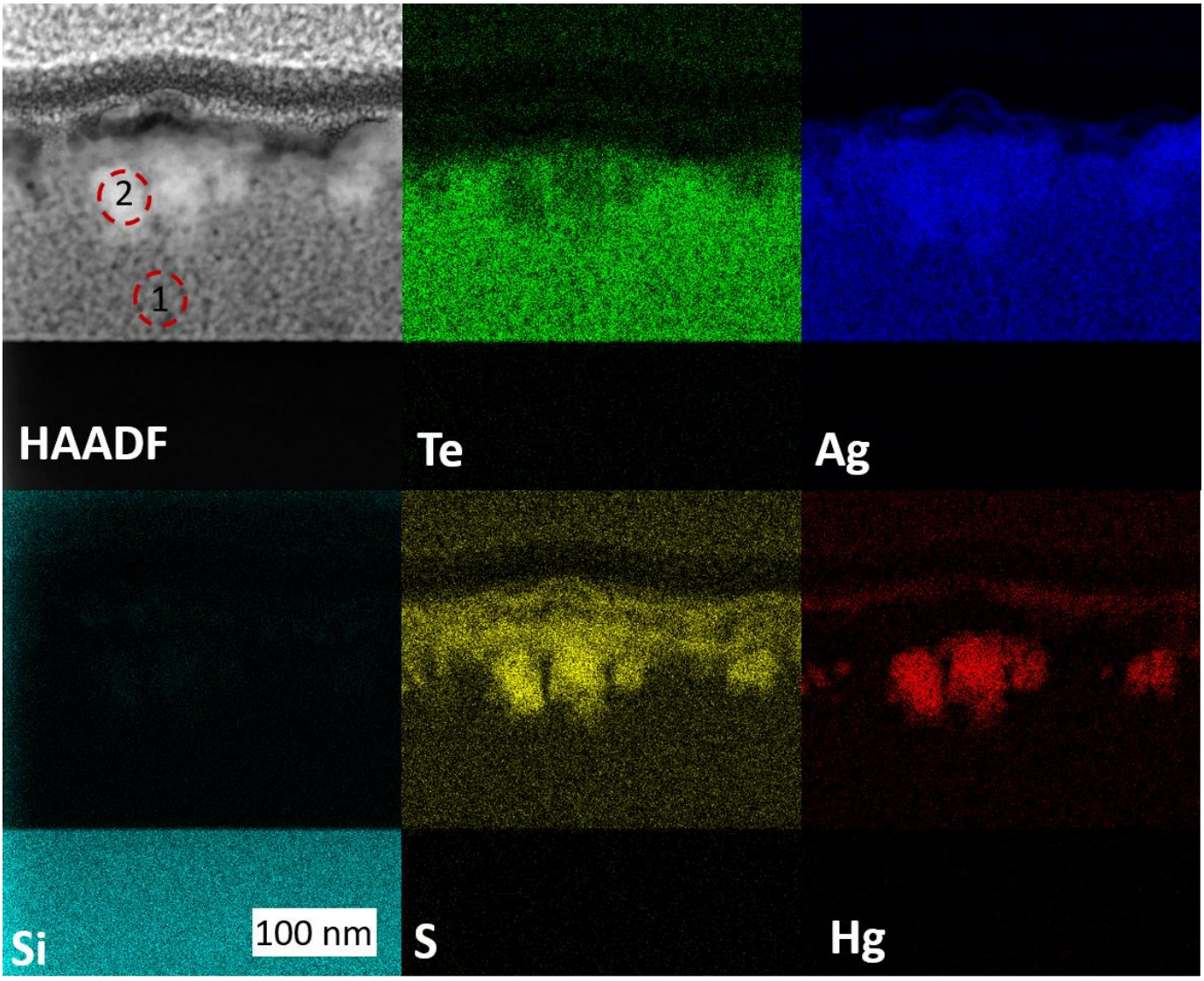


***Figure 4*** *STEM-HAADF image of a Si wafer coated with 200 nm of HgTe NCs, coated with 80 nm of Ag, top of the image is made of Pt coating used for FIB slicing.*

Because Ag deposition on HgTe appears as an alternative way to form $Ag_2Te$ layer we tested the possibility to build the initial diode while replacing the $Ag_2Te$ NC layer by an evaporation step of Ag. If ever successful, the method would simplify the overall fabrication of the diode stack by reducing the number of spin coatings and associated constraint of using orthogonal solvent at each step. Though the obtained diode still presents a rectifying IV curve, the overall photocurrent appears drastically reduced, see Figure S14.

## CONCLUSION

To summarize, we have screened the use of metallic grids as a possible strategy to replace TCO electrode while targeting the design of short and mid-wave infrared diodes based on HgTe NCs. Among tested candidates, Al is the only one preserving the electrical performances. Raman, XRD, XPS and EDX mapping bring consistent evidence that Ag coupled to HgTe experiences a dramatic cation exchange process which occurs without extra thermal activation and over the whole NC film. HgTe films transform into $Ag_2Te$ while the released Hg is metallic and forms an amalgam with remaining silver. This work points out dramatic chemical changes that can happen when coupling an HgTe NCs layer to a metallic thin film and we can anticipate that Ag will not be the only metal

concerned by this transformation. On the other hand, the massive use of gold for this diode is justified since we observe a good chemical stability in this case.

## SUPPORTING INFORMATION

Supporting Information include details about (i) transparency of FTO electrode (i*i*) IV curve for diode based on metallic grid, (*iii*) diffraction data for Ag on HgTe, (*iv*) core level analysis for XPS data, (*v*) EDX mapping for HgTe coupled to Au and (*vi*) electrical characterization of diode in which $Ag_2Te$ is replaced by Ag.


## ACKNOWLEDGEMENTS

We thank Mathieu G. Silly and synchrotron Soleil for enabling additional measurement at review stage. The project is supported by ERC grant blackQD (grant n° 756225) and AQDtive (grant n°101086358). We acknowledge the use of clean-room facilities from the “Centrale de Proximité Paris-Centre”. This work was supported by Agence Nationale de la recherche through the grants Copin (ANR-19-CE24-0022), Frontal (ANR-19-CE09-0017), Graskop (ANR-19-CE09-0026), NITQuantum (ANR-20-ASTR-0008), Bright (ANR-21-CE24-0012), MixDFerro (ANR-21-CE09-0029), Quicktera (ANR-22-CE09-0018) and Operatwist (ANR-22-CE09-0037-01).


## CONFLICT OF INTEREST

The authors declare no competing financial interest.

## REFERENCES


(1) Gréboval, C.; Chu, A.; Goubet, N.; Livache, C.; Ithurria, S.; Lhuillier, E. Mercury Chalcogenide Quantum Dots: Material Perspective for Device Integration. *Chem. Rev.* **2021**, *121* (7), 3627–3700. https://doi.org/10.1021/acs.chemrev.0c01120.

(2) Gréboval, C.; Darson, D.; Parahyba, V.; Alchaar, R.; Abadie, C.; Noguier, V.; Ferré, S.; Izquierdo, E.; Khalili, A.; Prado, Y.; et al. Photoconductive Focal Plane Array Based on HgTe Quantum Dots for Fast and Cost-Effective Short-Wave Infrared Imaging. *Nanoscale* **2022**, *14* (26), 9359–9368. https://doi.org/10.1039/D2NR01313D.

(3) Zhang, S.; Bi, C.; Qin, T.; Liu, Y.; Cao, J.; Song, J.; Huo, Y.; Chen, M.; Hao, Q.; Tang, X. Wafer-Scale Fabrication of CMOS-Compatible Trapping-Mode Infrared Imagers with Colloidal Quantum Dots. *ACS Photonics* **2023**, *10* (3), 673–682. https://doi.org/10.1021/acsphotonics.2c01699.

(4) Steckel, J. S.; Josse, E.; Pattantyus-Abraham, A. G.; Bidaud, M.; Mortini, B.; Bilgen, H.; Arnaud, O.; Allegret-Maret, S.; Saguin, F.; Mazet, L.; et al. 1.62 µm Global Shutter Quantum Dot Image Sensor Optimized for Near and Shortwave Infrared. In *2021 IEEE International Electron Devices Meeting (IEDM)*; IEEE: San Francisco, CA, USA, 2021; p 23.4.1-23.4.4. https://doi.org/10.1109/IEDM19574.2021.9720560.

(5) Maniyara, R. A.; Graham, C.; Paulillo, B.; Bi, Y.; Chen, Y.; Herranz, G.; Baker, D. E.; Mazumder, P.; Konstantatos, G.; Pruneri, V. Highly Transparent and Conductive ITO Substrates for near Infrared Applications. *APL Mater.* **2021**, *9* (2), 021121. https://doi.org/10.1063/5.0040864.

(6) Qu, J.; Weis, M.; Izquierdo, E.; Mizrahi, S. G.; Chu, A.; Dabard, C.; Gréboval, C.; Bossavit, E.; Prado, Y.; Péronne, E.; et al. Electroluminescence from Nanocrystals above 2 µm. *Nat. Photonics* **2022**, *16* (1), 38–44. https://doi.org/10.1038/s41566-021-00902-y.

(7) Shen, X.; Peterson, J. C.; Guyot-Sionnest, P. Mid-Infrared HgTe Colloidal Quantum Dot LEDs. *ACS Nano* **2022**, *16* (5), 7301–7308. https://doi.org/10.1021/acsnano.2c01694.

(8) Livache, C.; Martinez, B.; Goubet, N.; Gréboval, C.; Qu, J.; Chu, A.; Royer, S.; Ithurria, S.; Silly, M. G.; Dubertret, B.; et al. A Colloidal Quantum Dot Infrared Photodetector and Its Use for Intraband Detection. *Nat. Commun.* **2019**, *10* (1), 2125. https://doi.org/10.1038/s41467-019-10170-8.
(9) Galagan, Y.; Coenen, E. W. C.; Sabik, S.; Gorter, H. H.; Barink, M.; Veenstra, S. C.; Kroon, J. M.; Andriessen, R.; Blom, P. W. M. Evaluation of Ink-Jet Printed Current Collecting Grids and Busbars for ITO-Free Organic Solar Cells. *Sol. Energy Mater. Sol. Cells* **2012**, *104*, 32–38. https://doi.org/10.1016/j.solmat.2012.04.039.
(10) Lim, J. W.; Lee, Y. T.; Pandey, R.; Yoo, T.-H.; Sang, B.-I.; Ju, B.-K.; Hwang, D. K.; Choi, W. K. Effect of Geometric Lattice Design on Optical/Electrical Properties of Transparent Silver Grid for Organic Solar Cells. *Opt. Express* **2014**, *22* (22), 26891. https://doi.org/10.1364/OE.22.026891.
(11) Choi, Y.; Kim, D.; Do, E. C.; Kim, D.; Mun, J.; Lee, J. W.; Lee, Y.; Kim, Y. G. Interdigitated Front Contact Crystalline Silicon Solar Cell. *Sol. Energy* **2014**, *100*, 94–101. https://doi.org/10.1016/j.solener.2013.12.007.
(12) Gupta, D. K.; Langelaar, M.; Barink, M.; Van Keulen, F. Optimizing Front Metallization Patterns: Efficiency with Aesthetics in Free-Form Solar Cells. *Renew. Energy* **2016**, *86*, 1332–1339. https://doi.org/10.1016/j.renene.2015.09.071.
(13) Dang, T. H.; Abadie, C.; Khalili, A.; Gréboval, C.; Zhang, H.; Prado, Y.; Xu, X. Z.; Gacemi, D.; Descamps-Mandine, A.; Ithurria, S.; et al. Broadband Enhancement of Mid-Wave Infrared Absorption in a Multi-Resonant Nanocrystal-Based Device. *Adv. Opt. Mater.* **2022**, *10* (9), 2200297. https://doi.org/10.1002/adom.202200297.
(14) Yang, J.; Lv, Y.; He, Z.; Wang, B.; Chen, S.; Xiao, F.; Hu, H.; Yu, M.; Liu, H.; Lan, X.; et al. $Bi_2S_3$ Electron Transport Layer Incorporation for High-Performance Heterostructure HgTe Colloidal Quantum Dot Infrared Photodetectors. *ACS Photonics* **2023**. https://doi.org/10.1021/acsphotonics.2c01145.
(15) Rastogi, P.; Izquierdo, E.; Gréboval, C.; Cavallo, M.; Chu, A.; Dang, T. H.; Khalili, A.; Abadie, C.; Alchaar, R.; Pierini, S.; et al. Extended Short-Wave Photodiode Based on CdSe/HgTe/$Ag_2$Te Stack with High Internal Efficiency. *J. Phys. Chem. C* **2022**, *126* (32), 13720–13728. https://doi.org/10.1021/acs.jpcc.2c02044.
(16) Gréboval, C.; Izquierdo, E.; Abadie, C.; Khalili, A.; Cavallo, M.; Chu, A.; Dang, T. H.; Zhang, H.; Lafosse, X.; Rosticher, M.; et al. HgTe Nanocrystal-Based Photodiode for Extended Short-Wave Infrared Sensing with Optimized Electron Extraction and Injection. *ACS Appl. Nano Mater.* **2022**, *5* (6), 8602–8611. https://doi.org/10.1021/acsanm.2c02103.
(17) Beberwyck, B. J.; Surendranath, Y.; Alivisatos, A. P. Cation Exchange: A Versatile Tool for Nanomaterials Synthesis. *J. Phys. Chem. C* **2013**, *117* (39), 19759–19770. https://doi.org/10.1021/jp405989z.
(18) Danhel, A.; Ligmajer, F.; Sikola, T.; Walcarius, A.; Fojta, M. Electrodeposition of Silver Amalgam Particles on ITO – Towards Novel Electrode Material. *J. Electroanal. Chem.* **2018**, *821*, 53–59. https://doi.org/10.1016/j.jelechem.2017.12.008.
(19) Ligmajer, F.; Horák, M.; Šikola, T.; Fojta, M.; Daňhel, A. Silver Amalgam Nanoparticles and Microparticles: A Novel Plasmonic Platform for Spectroelectrochemistry. *J. Phys. Chem. C* **2019**, *123* (27), 16957–16964. https://doi.org/10.1021/acs.jpcc.9b04124.
(20) Sangaonkar, G. M.; Desai, M. P.; Dongale, T. D.; Pawar, K. D. Selective Interaction between Phytomediated Anionic Silver Nanoparticles and Mercury Leading to Amalgam Formation Enables Highly Sensitive, Colorimetric and Memristor-Based Detection of Mercury. *Sci. Rep.* **2020**, *10* (1), 2037. https://doi.org/10.1038/s41598-020-58844-4.
(21) Clarysse, J.; Moser, A.; Yarema, O.; Wood, V.; Yarema, M. Size- and Composition-Controlled Intermetallic Nanocrystals via Amalgamation Seeded Growth. *Sci. Adv.* **2021**, *7* (31), eabg1934. https://doi.org/10.1126/sciadv.abg1934.
(22) Son, D. H.; Hughes, S. M.; Yin, Y.; Paul Alivisatos, A. Cation Exchange Reactions in Ionic Nanocrystals. *Science* **2004**, *306* (5698), 1009–1012. https://doi.org/10.1126/science.1103755.
(23) De Trizio, L.; Manna, L. Forging Colloidal Nanostructures via Cation Exchange Reactions. *Chem. Rev.* **2016**, *116* (18), 10852–10887. https://doi.org/10.1021/acs.chemrev.5b00739.

(24) Zhang, J.; Chernomordik, B. D.; Crisp, R. W.; Kroupa, D. M.; Luther, J. M.; Miller, E. M.; Gao, J.; Beard, M. C. Preparation of Cd/Pb Chalcogenide Heterostructured Janus Particles *via* Controllable Cation Exchange. *ACS Nano* **2015**, *9* (7), 7151–7163. https://doi.org/10.1021/acsnano.5b01859.
(25) Pietryga, J. M.; Werder, D. J.; Williams, D. J.; Casson, J. L.; Schaller, R. D.; Klimov, V. I.; Hollingsworth, J. A. Utilizing the Lability of Lead Selenide to Produce Heterostructured Nanocrystals with Bright, Stable Infrared Emission. *J. Am. Chem. Soc.* **2008**, *130* (14), 4879–4885. https://doi.org/10.1021/ja710437r.
(26) Dufour, M.; Izquierdo, E.; Livache, C.; Martinez, B.; Silly, M. G.; Pons, T.; Lhuillier, E.; Delerue, C.; Ithurria, S. Doping as a Strategy to Tune Color of 2D Colloidal Nanoplatelets. *ACS Appl. Mater. Interfaces* **2019**, *11* (10), 10128–10134. https://doi.org/10.1021/acsami.8b18650.
(27) Sahu, A.; Kang, M. S.; Kompch, A.; Notthoff, C.; Wills, A. W.; Deng, D.; Winterer, M.; Frisbie, C. D.; Norris, D. J. Electronic Impurity Doping in CdSe Nanocrystals. *Nano Lett.* **2012**, *12* (5), 2587–2594. https://doi.org/10.1021/nl300880g.
(28) Fedorov, V.; Ganshin, V.; Korkishko, Y. N. Formation of $Hg_xCd_{1-x}Te$ Layers by Ion Exchange. *Semicond. Sci. Technol.* **1991**, *6* (12), 1113.
(29) Fedorov, V. A.; Ganshin, V.; Korkishko, Y. N. Ion Exchange in II–VI Crystals: Thermodynamics, Kinetics, and Technology. *Phys. Status Solidi A* **1993**, *139* (1), 9–65.
(30) Ackerman, M. M.; Chen, M.; Guyot-Sionnest, P. HgTe Colloidal Quantum Dot Photodiodes for Extended Short-Wave Infrared Detection. *Appl. Phys. Lett.* **2020**, *116* (8), 083502. https://doi.org/10.1063/1.5143252.
(31) Ackerman, M. M.; Tang, X.; Guyot-Sionnest, P. Fast and Sensitive Colloidal Quantum Dot Mid-Wave Infrared Photodetectors. *ACS Nano* **2018**, *12* (7), 7264–7271. https://doi.org/10.1021/acsnano.8b03425.
(32) Keuleyan, S.; Lhuillier, E.; Guyot-Sionnest, P. Synthesis of Colloidal HgTe Quantum Dots for Narrow Mid-IR Emission and Detection. *J. Am. Chem. Soc.* **2011**, *133* (41), 16422–16424. https://doi.org/10.1021/ja2079509.
(33) Li, Q.; Zhang, J.; Zheng, Q.; Guo, W.; Cao, J.; Jin, M.; Zhang, X.; Li, N.; Wu, Y.; Ye, X.; et al. Pressure-Induced Superconductivity in HgTe Single-Crystal Film. *Adv. Sci.* **2022**, *9* (18), 2200590. https://doi.org/10.1002/advs.202200590.
(34) Harika, V. K.; Kumar, V. B.; Gedanken, A. One-Pot Sonochemical Synthesis of Hg–Ag Alloy Microspheres from Liquid Mercury. *Ultrason. Sonochem.* **2018**, *40*, 157–165. https://doi.org/10.1016/j.ultsonch.2017.07.008.
(35) Kashida, S. Electronic Structure of Ag2Te, Band Calculation and Photoelectron Spectroscopy. *Solid State Ion.* **2002**, *148* (1–2), 193–201. https://doi.org/10.1016/S0167-2738(02)00046-2.
(36) Panaccione, G.; Cautero, G.; Cautero, M.; Fondacaro, A.; Grioni, M.; Lacovig, P.; Monaco, G.; Offi, F.; Paolicelli, G.; Sacchi, M.; et al. High-Energy Photoemission in Silver: Resolving d and Sp Contributions in Valence Band Spectra. *J. Phys. Condens. Matter* **2005**, *17* (17), 2671–2679. https://doi.org/10.1088/0953-8984/17/17/015.
(37) Sato, K.; Hirata, K.; Singh, S.; Kuga, K.; Ogawa, F.; Matsunami, M.; Takeuchi, T. Electronic Structure of Silver Chalcogenides Investigated by Hard X-Ray Photoemission Spectroscopy and Density Functional Theory Calculations. *J. Appl. Phys.* **2022**, *132* (4), 045104. https://doi.org/10.1063/5.0095987.

**TOC graphic**